Nano Research

Open Access

Research Article

Multi-resolved imaging of electrocatalytic and photoelectrocatalytic oxygen evolution processes on two-dimensional transition metal dichalcogenides

Lisi Wen[1,§], Zhuojun Duan[2,§], Jiayuan Cheng[2], Houkai Chen[1], Bo Liu[3], Song Liu[2]✉, and Rui Hao[1]✉

[1] *Department of Chemistry, Research Center for Chemical Biology and Omics Analysis, Shenzhen Key Laboratory of Functional Proteomics, Southern University of Science and Technology, Shenzhen 518055, China*
[2] *State Key Laboratory of Chemo and Biosensing, College of Chemistry and Chemical Engineering, Hunan University, Changsha 410082, China*
[3] *College of Mechanical Vehicle Engineering, Hunan University, Changsha 410082, China*
[§] *Lisi Wen and Zhuojun Duan contributed equally to this work.*

Cite this article: *Nano Research*, **2026**, *19*, 94908340. https://doi.org/10.26599/NR.2026.94908340

ABSTRACT: The efficient conversion of solar energy into chemical fuels, using solar-energy-generated electricity to drive electrocatalytic (EC) or photoelectrocatalytic (PEC) water splitting, is still a grand challenge in sustainable energy due to the sluggish oxygen evolution reaction (OER). Two-dimensional (2D) semiconductors are promising catalysts in both cases, yet their performance is governed by a complex and heterogeneous landscape of atomic-scale defects that remains convoluted. Here, a multi-resolved imaging strategy, combining *in situ* electrochemiluminescence (ECL), photoinduced ECL, and photoluminescence imaging modes with *ex situ* scanning transmission electron microscopy (STEM) analysis, was employed to provide comprehensive insights into the dynamic heterogeneous relationship between catalytic activity, carrier behaviors and active sites on 2D semiconducting materials. By investigating pristine and annealed monolayer MoS_2, we establish a direct link between the distribution of specific defect types and their unique influence on catalytic activity and carrier behavior. We've identified molybdenum vacancies (V_{Mo}) as bifunctional active sites for both EC and PEC OER, while sulfur vacancies (V_S), while not primary catalytic centers, uniquely enhance PEC efficiency. This work provides a powerful methodology for elucidating complex, dynamic catalytic mechanisms, paving the way for the defect-level engineering of high-performance 2D materials-based catalysts.

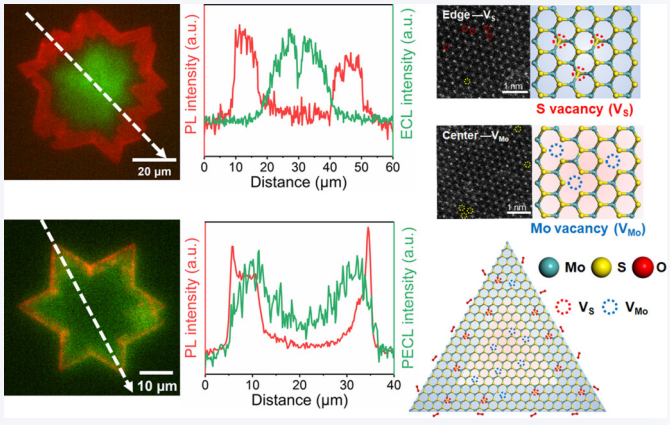

KEYWORDS: multi-resolved imaging, *in situ* photoluminescence (PL) imaging, *in situ* photoinduced electrochemiluminescence (PECL) imaging, *in situ* electrochemiluminescence (ECL) imaging, oxygen evolution reaction

1 Introduction

Electrocatalytic and photoelectrocatalytic water splitting are essential for generating green and sustainable fuels from renewable energy sources [1, 2]. The oxygen evolution reaction (OER), functioning as the anodic half-reaction, restricts the water-splitting performance owing to the considerable overpotential caused by its slow reaction kinetics [3]. Therefore, high-performance catalysts are crucial for achieving affordable and scalable water (photo)electrolyzers [4]. Recently, two-dimensional (2D) transition metal dichalcogenides (TMDs) have emerged as compelling platforms for both electrocatalysis [5] and photoelectrocatalysis [6] due to layer-tunable band gaps and rich and diverse catalytically active defect sites [7, 8].While defect engineering is a potent strategy for enhancing activity, progress is hampered by a lack of fundamental understanding. The performance of any given TMD

Received: September 7, 2025; **Revised:** November 18, 2025
Accepted: December 14, 2025

✉Address correspondence to Song Liu, liusong@hnu.edu.cn; Rui Hao, haor@sustech.edu.cn

flake is dictated by a heterogeneous distribution of various point defects (e.g., metal or chalcogen vacancies), but their individual contributions remain obscured. This leads to a challenging question in the field: Are the active sites for electrocatalysis and photoelectrocatalysis identical, and how do specific defects differentially modulate charge carrier dynamics to favor one pathway over the other?

Answering this requires comprehensive *in situ*/*operando* characterization with both spatiotemporal and chemical resolutions at the single-flake level. Several imaging techniques have recently been developed to investigate dynamic and heterogeneous processes at the electrochemical interfaces, for instance, scanning probe techniques [9] like scanning electrochemical cell microscopy (SECCM) [10, 11], scanning electrochemical microscopy (SECM) [12], can map (photo)electrochemical activity with high spatial resolution; however, their serial nature limits temporal resolution.

Widefield electrochemical imaging could be achieved with optical microscopy-based methods [13], including single-molecule labeling [14–16], dark-field microscopy (DFM) [17–19], and surface plasmon resonance microscopy (SPRM) [20, 21], for mapping dynamic, heterogeneous electrochemical events on a global scale. Specifically, electrochemiluminescence microscopy (ECLM), which does not require external light, offers significant advantages such as low background, high sensitivity, and high-resolution imaging of reactive species formed at the electrode surface [22, 23]. For instance, the electrocatalytic activities of ZnO nanocrystals [24] and Au nanoplate [25] have been visualized, revealing facet-dependent intensity variations.

Photoelectrocatalytic activity can be monitored via scanning-based photocurrent mapping [26] or molecular labeling methods [27–30]. Single-molecule fluorescence techniques could monitor the photoelectrocatalytic process with high spatiotemporal resolution. However, the required laser excitation for fluorescence might also excite narrow band gap materials like MoS_2 [30], causing interference. On the other side, photoinduced ECL (PECL), where photogenerated carriers drive the chemiluminescent reaction, provides a direct route to image photoelectrocatalytic processes [31–34] with no requirement for excitation of the probing molecules, exhibiting excellent potential for *in situ* imaging [35] of photoelectrocatalytic processes on various 2D semiconductors.

Furthermore, photoluminescence (PL), a fundamental light emission process induced by photon excitation in semiconductors, serves as a nondestructive tool for studying photocatalysis [36]. Because PL is closely coupled with photogenerated carrier kinetics, PL imaging provides essential insights into the electronic and optical properties of 2D semiconductors [37–39]. Thus, *in situ* PL mapping could be beneficial for investigating the carrier behavior of 2D semiconductors during photoelectrochemical reactions.

Despite the valuable information being accessible, a single imaging technique offers a limited perspective, hindering a comprehensive understanding of the electrochemical kinetics of individual entities [40]. Multimodal *in situ* imaging provides multi-perspective insight into the same electrochemical processes with high resolution at the single-entity level [3]. In this case, the high compatibility across diverse optical imaging modalities makes them ideal candidates for simultaneously resolving spatial, temporal, and chemical heterogeneities at electrochemical interfaces [41]. For instance, the heterogenous dynamic evolution of electrocatalysis and electrocatalytic reaction could be resolved simultaneously with multimodal optical imaging, e.g. ECL/Vis-absorption [42] and interference/fluorescence [43], providing key insights that would otherwise be inaccessible. The detailed atomic defect of 2D materials could only be accessed with scanning transmission electron microscopy (STEM). However, it is extremely challenging for the method to provide *in situ* information, not mentioning monitoring the "electron invisible" catalytic reactions at single sites. Therefore, correlating *in situ* dynamic chemical changes with *ex situ* atomic characterization could greatly benefit disentangling complex reaction mechanisms at the electrochemical interface.

In this study, we present a spatially, temporally, and chemically multi-resolved *in situ* imaging technique by integrating *in situ* ECL, PECL, and PL imaging and *ex situ* STEM to comprehensively investigate the electrocatalytic and photoelectrocatalytic OER activity of 2D semiconducting TMDs. The ECL imaging offers detailed information on active site distribution during electrocatalytic processes, the PECL mode characterizes the heterogeneous activity distribution of photoelectrocatalytic processes, while PL imaging monitors the separation and transfer of the carriers. Carrier effects on electrocatalytic and photoelectrocatalytic OER can be directly visualized. The STEM analysis was used to provide detailed information at atomic level. With the multi-resolved imaging approach, pristine and annealed monolayer MoS_2 flakes were investigate *in situ*, showing a distinct heterogeneous electrocatalytic/photoelectrocatalytic/carrier distribution. Correlated with STEM analysis, it was found that molybdenum vacancy (V_{Mo}) acts as the active site for catalyzing both electrocatalytic and photocatalytic OER, and the presence of sulfur vacancy (V_S) can improve photoelectrocatalytic efficiency. This multi-resolved imaging approach provides a comprehensive understanding of the structure and activity of 2D semiconductor materials for electro- and photoelectro-catalytic applications.

2 Results and discussion

2.1 Multimodal imaging of exfoliated TMDs nanosheets during OER

We developed a multimodal imaging technique to characterize the active sites of TMDs during electrocatalytic and photoelectrocatalytic OERs (Fig. 1). The working electrode (WE) consisted of silane-modified indium tin oxide (ITO) coated with exfoliated nanosheets of n-type MoS_2 or p-type WSe_2 (Fig. S1(a) in the Electronic Supplementary Material (ESM)). These exfoliated TMDs had a thickness of 25–40 nm (Fig. S2 in the ESM). To observe surface signals, a three-electrode sandwich electrochemical cell was designed for microscopic observation (Fig. S3 in the ESM).

Luminol was used as a reporter molecule to study the effect of applied potential on semiconductor catalysis. In an alkaline medium, the superoxide radical anion ($O_2^{\bullet-}$) produced during water oxidation reacts with the luminol radical anion ($L^{\bullet-}$), the oxidation product of luminol, resulting in excited-state aminophthalic acid [24] (Fig. S4(a) in the ESM). ECL emission occurs when excited-state species return to their ground state (ECL mode, Fig. 1(a)).

Narrow band gap semiconductors, such as MoS_2 (E_g = 1.30 eV) [44] and WSe_2 (E_g = 1.25 eV) [45], can be excited by irradiation with wavelengths ranging from infrared to ultraviolet, promoting electrons (e^-) from the valence band (VB) to the conduction band (CB), creating different excited states. Holes (h^+) are generated simultaneously in the VB. Most photogenerated carriers recombine to produce PL [36] (PL mode, Fig. 1(b)), while

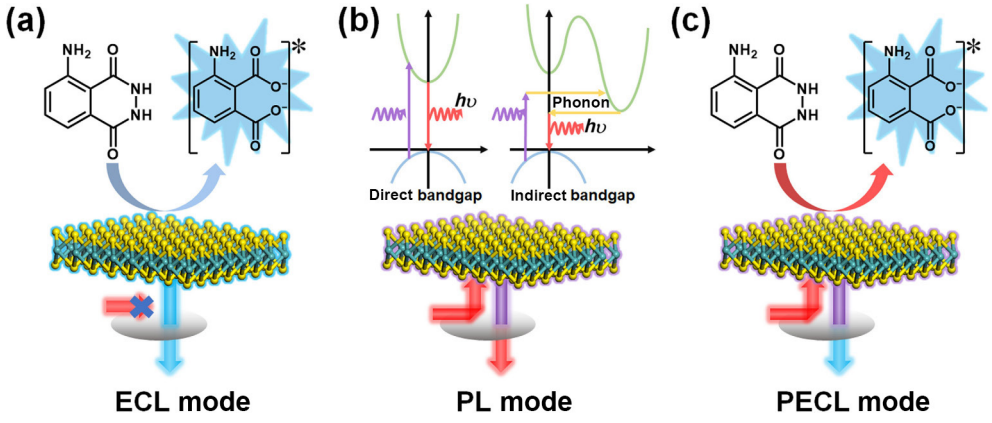

Figure 1 Schematic illustration of different modes. (a) ECL, (b) PL, and (c) PECL modes.

some undergo charge transfer at the semiconductor-liquid interface. Application of a positive bias drives photogenerated h^+ to the interface, oxidizing luminol and water to generate $L^{\bullet-}$ and $O_2^{\bullet-}$, respectively, which further react to form excited-state aminophthalic acid [46] (Fig. S4(b) in the ESM). When the excited-state species return to the ground state, PECL emissions are observed (PECL mode, Fig. 1(c)). This mechanism was verified by the significant suppression of PECL upon introduction of the superoxide scavenger p-benzoquinone (pBQ) [47, 48], confirming that the superoxide-mediated pathway predominates over direct hole oxidation in driving light emission (Fig. S5 in the ESM).

Under these experimental conditions (strongly alkaline electrolyte, pH = 13), the very high concentration of OH^- competitively occupies the active surface sites, making the adsorption of luminol negligible [49]. Therefore, the overall ECL intensity in our system primarily reflects OER-related reactive oxygen species generation and interfacial charge -transfer dynamics rather than differences in luminol adsorption across surface sites. To distinguish between the PL and PECL signals, appropriate filters must be placed in front of the Electron Multiplying Charge-Coupled Device (EMCCD) (Fig. S6 in the ESM).

The modified ITO electrode coated with the exfoliated p-type WSe_2 was analyzed in three modes (Fig. 2(a) and Fig. S7 in the ESM). Cyclic voltammetry (CV) curves showed no significant differences across modes, with negligible laser-induced anodic photocurrent (Fig. S8 in the ESM). Additionally, a characteristic anodic peak at approximately 0.7 V was consistently observed, which we attribute to the intrinsic oxidation of WSe_2. Control experiments confirm that this peak appears only in the presence of WSe_2 and is absent in luminol-only electrolyte (Fig. S9 in the ESM), demonstrating that it originates from the material's own oxidative transition rather than luminol-related processes.

In PL imaging mode, multilayer WSe_2, an indirect band gap semiconductor, initially exhibited low PL efficiency (Fig. S10(a) in the ESM). As the potential increased, the material progressively oxidized and corroded, starting from the edges (Fig. S11 in the ESM). A PL signal emerged at the edge at approximately 0.8 V, peaking at 1.0 V during the reverse scan (Fig. 2(c)). The ECL signal emerged at the edges at approximately 0.6 V. With increasing voltage, oxidation and corrosion of the material progressed (Fig. S11 in the ESM). The ECL signal corresponded to the corrosion process, reaching a maximum at 0.69 V and fluctuating as corrosion continued. The PECL signal closely followed the same potential-dependent trend as the ECL signal. The slightly higher initial intensity of PECL may be attributed to intrinsic variations among individual nanosheets—such as differences in size or morphology—or alternatively, to a limited contribution from photogenerated carriers induced by the laser illumination.

Similarly, exfoliated n-type MoS_2 was investigated in three modes (Fig. 2(b) and Fig. S12 in the ESM). CV experiments showed consistent curve shapes across modes, but the PL/PECL modes exhibited higher currents due to laser-induced photocurrent (Fig. S13 in the ESM). A small initial laser spot (~ 80 μm) caused no significant shift in onset potential, as the limited carrier density generated by localized illumination produced a response representative of the substrate-modified ITO. Whereas, under a 2 mm laser spot that homogeneously excited the nanosheets across the entire reaction area, shifting the onset potential from 0.6 to 0.05 V and reflecting the true electrochemical response of the material (Fig. S14 in the ESM).

In PL imaging, multilayer MoS_2, an indirect band gap semiconductor comparable to multilayer WSe_2, initially exhibited low PL efficiency (Fig. S10(b) in the ESM). With increasing potential, the material gradually oxidized and corroded from the edge (Fig. S15 in the ESM). A PL signal emerged at the edge at 0.15 V, peaking at 1.4 V (Fig. 2(d)). The edges were typically thinner than the basal plane and hosted a higher density of structural defects. These defect sites created localized electronic states that served as preferential centers for radiative recombination, thus promoting the initial PL emission at these sites. During the reverse scan, the PL intensity decreased but remained higher than the initial value. The ECL signal initiated at the edge at 0.8 V, peaked at 1.08 V, then decreased. The PECL signal appeared at −0.2 V, remained stable in the range of 0.1 to 1.4 V with slight fluctuations, and disappeared during the reverse scan.

When comparing the changes in signal intensity with potential for p-type WSe_2 and n-type MoS_2 across the three imaging modes, no significant differences exist between the ECL and PECL signals for p-type WSe_2. However, n-type MoS_2 had a significantly earlier PECL onset (~ 1.0 V earlier than ECL). In the anode reaction, the laser had negligible effects on the OER of p-type WSe_2 but significantly promoted the OER of n-type MoS_2.

Under dark conditions, charge transfer at the semiconductor-electrolyte interface was governed by majority carriers, making p-type semiconductors prone to oxidation reactions, whereas n-type semiconductors favor reduction [50]. Consequently, the onset potential for oxidation in the p-type WSe_2 appeared earlier than

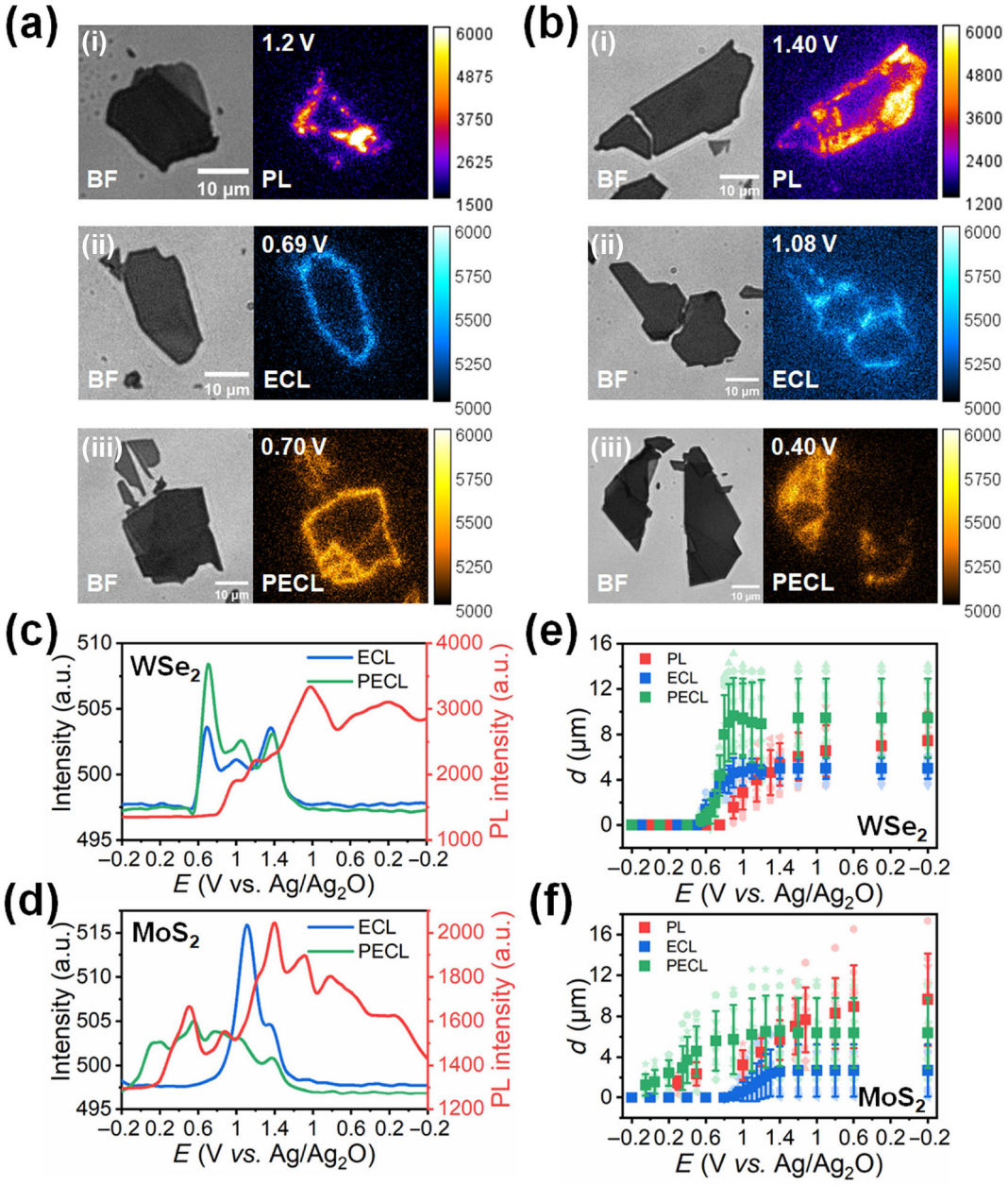

Figure 2 *In situ* imaging of WSe_2 and MoS_2 in different modes. (a) Bright field (BF) images (left) and corresponding (i) PL, (ii) ECL, and (iii) PECL mode images (right) for WSe_2. (b) BF images (left) and corresponding (i) PL, (ii) ECL, and (iii) PECL modes images (right) for MoS_2. Intensity vs. potential curve of (c) WSe_2 and (d) MoS_2 in PL (red), ECL (blue), PECL (green) modes. Corrosion distance vs. potential curve of (e) WSe_2 and (f) MoS_2 in PL (red), ECL (blue), PECL (green) modes.

that in the n-type MoS_2. For exfoliated n-type MoS_2, oxidation was restricted to partially p-doped S-edges, where h^+ accumulation could occur, as confirmed by ECL signals observed at specific edge sites (Fig. S12(b) in the ESM).

Under illumination, photogenerated electron–hole pairs disrupt thermal equilibrium, resulting in separate quasi-Fermi levels for e^- ($E_{f,n}$) and h^+ ($E_{f,p}$) [34]. In p-type semiconductors, the substantial increase in photogenerated e^- caused $E_{f,n}$ to shift upward, enhancing the reduction capability. In n-type semiconductors, the increase in photogenerated h^+ resulted in a downward shift in $E_{f,p}$, significantly improving the oxidation efficiency. Therefore, illumination exerted a minimal effect on p-type WSe_2 but markedly advanced the onset potential for oxidation in n-type MoS_2.

In addition, the PL signal displayed distinct potential-dependent characteristics. The PL intensity of p-type WSe_2 remained nearly constant during reverse scans, whereas that of n-type MoS_2 increased initially and gradually decreased during the reverse scan, yet remained higher than the initial level. The onset potential of the PL signal appeared approximately 200 mV later than that of the PECL signal for both materials, which can be attributed to the fact that PL emission occurs only after oxidation and corrosion have taken place [51], while PECL emission proceeds simultaneously with these processes.

Previous studies had shown that applied voltage affected PL signal intensity by regulating the Fermi level (E_f), with the PL quantum yield reaching its maximum when E_f was equidistant from the CB and VB [52]. According to the semiconductor energy band structure, the E_f of p-type WSe_2 lay near the VB. When a

positive potential was applied, the enrichment of positive charges shifted E_f closer to the VB, promoting the formation of positive trions and reducing the PL quantum yield [53]. However, this reduction was counteracted by multiple synergistic effects: the oxidation-induced layer thinning of multilayer of multilayer WSe_2 to few-layer or near-monolayer thickness shifted its band structure toward a more direct-gap character, thereby enhancing the PL emission [50]. Simultaneously, oxidation-induced vacancy doping modulated the PL quantum yield, causing signal fluctuations during the reverse scan [36]. These combined effects resulted in no significant decrease in signal intensity.

The E_f of n-type MoS_2 was located near the CB. Positive potential application removed excess e^-, shifting the E_f toward the VB. This transition transformed the negative trions into neutral excitons, a key factor enhancing enhanced the PL quantum yield [53]. Concurrently, oxidation converted multilayer MoS_2 to few-layer or near-monolayer thickness shifted its band structure toward a more direct-gap character [50] and further contributing to PL enhancement. The vacancy doping introduced during oxidation also contributed to signal fluctuations. In the reverse scanning process, neutral excitons reverted to negative trions, reducing PL intensity. Nevertheless, the final PL intensity remained higher than the initial value due to the combined influence of defect-induced effects, and residual band structure alterations caused by oxidation.

To further investigate the corrosion behavior of the materials, corrosion rates were analyzed across the three imaging modes (Figs. 2(e) and 2(f)). The corrosion distances of 10 randomly selected points along the material edge were quantified during the reaction, based on the position of the luminous boundary (as shown in Figs. S16 and S17 in the ESM; additional *in situ* BF corrosion images are provided in Figs. S18 and S19 in the ESM). For p-type WSe_2, no significant difference in the initial corrosion rate was observed across the imaging modes. However, as the potential increased, the final corrosion distances in PL and PECL modes became significantly larger than those in ECL mode. For n-type MoS_2, the onset of corrosion occurred earlier, and the final corrosion extent was substantially greater under both PL and PECL modes compared to the ECL mode. These findings suggested that laser illumination promoted corrosion in both p-type WSe_2 and n-type MoS_2.

2.2 Multimodal imaging of pristine monolayer MoS_2 during the OER

To further investigate the distribution of catalytic sites in n-type 2D semiconductors during electrocatalysis and photoelectrocatalysis, monolayer MoS_2 was synthesized via chemical vapor deposition (CVD) and transferred to modified ITO substrates for subsequent imaging (Fig. S1(b) in the ESM). Owing to the thin nature of the monolayer MoS_2, the surface signals could be clearly captured. The sample was placed upright on an inverted microscope with a Pt wire as the CE and an Hg/HgO electrode as the RE (Fig. S20 in the ESM). A CV potential sweep ranging from −0.2 to 1.4 V was applied to explore the signal variations of pristine MoS_2 in three different imaging modes (Fig. S21 in the ESM). No significant differences were observed in the shapes of the CV curves across these modes, and the current signals in the PL and PECL modes were not significantly higher than those in the ECL mode. This can be explained by the sparse and inhomogeneous distribution of the CVD-grown MoS_2. In such a configuration, the faradaic current from the nanosheets is too low to be distinguished from the dominant capacitive background, while inefficient charge injection and poor collection of photogenerated carriers further diminish the modality-specific responses.

As a direct band gap semiconductor, monolayer MoS_2 exhibited a high PL quantum efficiency, and clear PL signals could be observed when no external potential is applied (Fig. S22 in the ESM). Notably, the PL signal at the edges was significantly stronger than at the center, suggesting the involvement of multiple excitonic processes. Previous studies have shown that the edges of MoS_2 monolayers typically terminate with Mo atoms [54, 55], where O_2 molecules from the atmosphere can be adsorbed. The O_2 molecules possess two singly occupied π^* orbitals (two unpaired electrons), capable of accepting two electrons [56]. By introducing p-doping, excess electrons from the intrinsic n-doping are neutralized, resulting in a transition from negative trions to neutral excitons [57, 58]. In addition, the adsorption of O_2 at the Mo edge suppresses electrostatic screening, many-body effects, and relevant nonradiative recombination processes owing to the lower emission energy of trions than that of the excitons, leading to enhanced PL signal at the edge.

When a positive potential was applied, an enhanced PL signal was observed across the entire material (Fig. 3(a)). However, this enhancement was more pronounced at the edges of the material than at the center, with the maximum intensity reaching at approximately 0.6 V, and subsequently stabilizing. Upon further increasing the potential to 0.8 V, oxidation and corrosion of the material were initiated at the center, as evidenced by the *in situ* BF imaging shown in Fig. S23(a) in the ESM, leading to a decrease and eventual disappearance of the PL signal from the central regions. The signal at the edges weakened and gradually decreased to its initial value (Fig. 3(d)). In addition, when the PL spectrum of the material was monitored as the potential was varied, no significant shift in the peak position was observed (Fig. S24 in the ESM), indicating that the electronic structure of the material remained relatively stable during this process.

Pristine MoS_2 synthesized via CVD is electron-rich, with its Fermi level positioned near the CB. Therefore, when a negative potential is applied, nonradiative recombination of trions becomes dominant, resulting in a lower quantum yield. In contrast, applying a positive potential reduces the background electron concentration, causing most quasiparticles to transform into neutral excitons [52]. Consequently, the radiative recombination rate of excitons increases, leading to a higher quantum yield. Excess positive charges accumulate at higher voltages. These charges can interact with excitons to form positive trions, which further increase the nonradiative recombination rate and subsequently decrease the PL intensity.

During electrocatalysis, pristine MoS_2 did not produce an ECL signal (Figs. 3(b) and 3(e)), which is consistent with the fact that n-type semiconductors generally do not exhibit catalytic activity at the anode [59]. In addition, no significant corrosion was observed during the electrocatalytic process (Fig. S23(b) in the ESM). However, during photoelectrocatalysis, pristine MoS_2 began to generate PECL signals at approximately 0.2 V, reaching a maximum intensity at approximately 0.8 V. Notably, these signals were confined to the center of the material (Figs. 3(c) and 3(d)). As the potential increased further, the center of the material progressively eroded, leading to a corresponding reduction and eventual disappearance of the PECL signal. A comparison of the PL signals revealed a complementary spatial distribution between the PECL and PL signals (Fig. 3(f)).

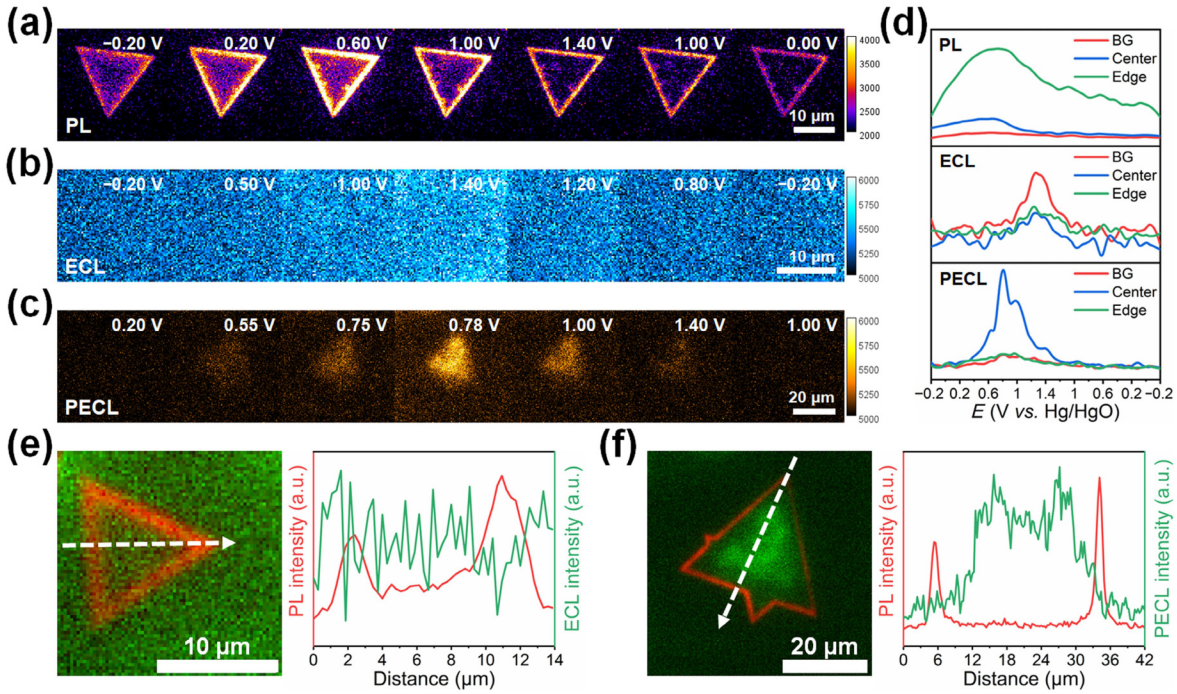

Figure 3 *In situ* imaging of pristine MoS_2 synthesized by CVD in different modes: (a) PL, (b) ECL, and (c) PECL. (d) Intensity vs. potential curves for different regions of pristine MoS_2 in PL (top), ECL (middle), and PECL (bottom) modes. BG: background signal on ITO. (e) Merged image and intensity profile along the white arrow in PL (red) and ECL (green) images. (f) Merged image and intensity profile along the white arrow in PL (red) and PECL (green) images.

2.3 Multimodal imaging of annealed monolayer MoS_2 during the OER

To further investigate the catalytically active sites of MoS_2, pristine MoS_2 was annealed at 400 °C in an Ar atmosphere to introduce additional vacancy sites. The annealed MoS_2 exhibited signal changes distinct from those of the pristine sample when subjected to a potential range of −0.2 to 1.4 V (Fig. 4 and Fig. S25 in the ESM). However, no significant differences were observed in the current curves among the three imaging modes (Fig. S26 in the ESM).

Similar to the pristine MoS_2, the annealed MoS_2 retained a monolayer structure, but the material was larger (Fig. S27 in the ESM). When no external voltage was applied, the material exhibited noticeable PL signals with an evident spatial distribution. The PL intensity was significantly stronger at the edges, whereas the center of the material exhibited nearly negligible PL signals (Fig. S27(b) in the ESM). This distribution could be attributed to the unique defects and vacancy sites generated during annealing.

Upon applying a positive potential, the PL signal of the annealed MoS_2 increased with increasing voltage, with a particularly significant enhancement observed at the edges of the material. This enhancement peaked at approximately 0.6 V (Figs. 4(a) and 4(d)). However, as the voltage increased, the edges underwent oxidation and corrosion (Fig. S28(a) in the ESM), decreasing the PL signal intensity, which eventually disappeared. In contrast, the PL signal at the center of the material remained unaffected throughout this process. This finding suggested that the edge regions were more sensitive to the applied potential under illumination than the center and underwent significant changes in their catalytic and optical properties. Furthermore, the PL spectrum of the material revealed no noticeable shift in peak position as the potential varies (Fig. S29 in the ESM), suggesting that the electronic structure of the material remained relatively unchanged throughout the process.

In contrast to pristine MoS_2, the annealed MoS_2 exhibited electrocatalytically active site, and the distribution of the photoelectrocatalytically active sites differed. In the ECL imaging mode, signals appeared at approximately 0.2 V, reaching their maximum at approximately 0.9 V before decreasing and disappearing (Figs. 4(b) and 4(d)). Notably, the ECL signals were confined to the center of the material and complemented the PL signals (Fig. 4(e)). In the PECL imaging mode, PECL signals emerged when a potential of −0.2 V was applied (Figs. 4(c) and 4(d)), predominantly concentrated at the edges, where the PL signal was more prominent (Fig. 4(f)). The PECL signal intensified with increasing voltage, reaching its maximum at 0.6 V. Beyond 0.6 V, the signal at the edges weakened as the material underwent oxidation and corrosion. In contrast, the center of the material experienced minimal oxidative corrosion, with PECL intensity peaking as the voltage increased to 1.0 V. Consequently, at approximately 0.8 V, the PECL intensity distribution appeared uniform across the material. Before applying a voltage of 0.8 V, the PECL intensity was stronger at the edges compared to the center, whereas after applying a voltage of 0.8 V, the PECL intensity in the center became more prominent than that at the edges.

To understand the differences in the distribution of active sites in CVD-synthesized MoS_2 during electrocatalysis and photoelectrocatalysis, the intrinsic properties of pristine and annealed MoS_2 were characterized. The PL mapping results were consistent with the PL imaging observations for both materials (Fig. S30(a) in the ESM), whereas no notable differences were observed between the edge and center regions in the Raman mapping results (Fig. S30(b) in the ESM). Notably, the uniform Raman mapping indicates minimal spatial variations in phonon modes, which helps exclude significant contributions from non-uniform stress induced by post-growth substrate interactions, as well as large-scale inhomogeneities in defect density or grain boundary effects that

could otherwise cause PL signal heterogeneity. STEM analysis confirmed that pristine MoS_2 did not exhibit any significant structural vacancies (Fig. 5(a)) and retained its intrinsic n-type semiconductor properties. Consequently, pristine MoS_2 lacked catalytic activity for the anode reaction in the dark, but demonstrated significant photoelectrocatalytic activity under illumination. In addition, the complementary nature of the PL and PECL signals could be attributed to attributed to the O_2 adsorption (Fig. 5(c)). On one hand, O_2 adsorption enhances PL emission by suppressing nonradiative recombination. On the other hand, it passivates the catalytically active edge sites, thereby inhibiting the charge transfer process necessary for PECL generation.

In contrast, the STEM analysis revealed that the annealed MoS_2 contained a large number of vacancies, with V_{Mo} predominantly concentrated at the center and a higher density of V_S along with fewer V_{Mo} distributed at the edges (Fig. 5(b)). The quenching of the PL signal at the center was attributed to V_{Mo}, which served as a trap for photogenerated carriers, effectively inhibiting the recombination of photogenerated e^- and h^+. In the PL mode, the intensity of the PL signal at the outermost edge of the annealed MoS_2 was higher than

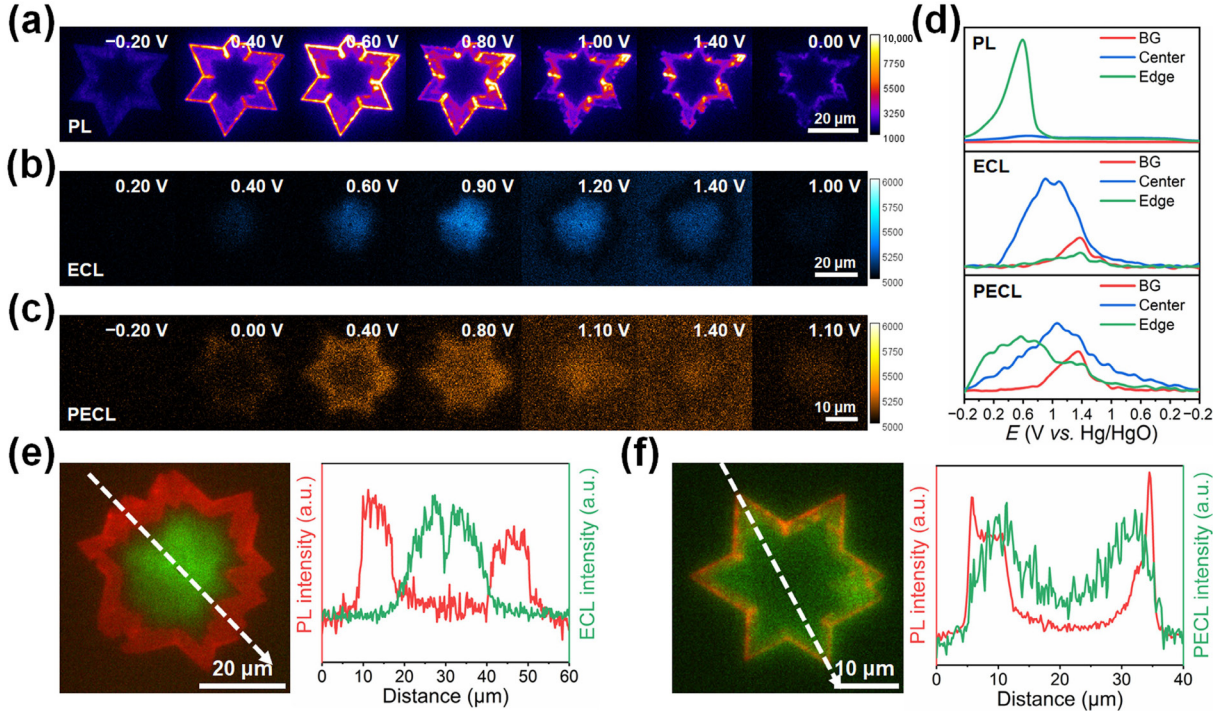

Figure 4 *In situ* imaging of annealed MoS_2 synthesized by CVD in different modes: (a) PL, (b) ECL, and (c) PECL. (d) Intensity vs. potential curves for different regions of annealed MoS_2 in PL (top), ECL (middle), and PECL (bottom) modes. BG: background signal on ITO. (e) Merged image and intensity profile along the white arrow in PL (red) and ECL (green) images. (f) Merged image and intensity profile along the white arrow in PL (red) and PECL (green) images.

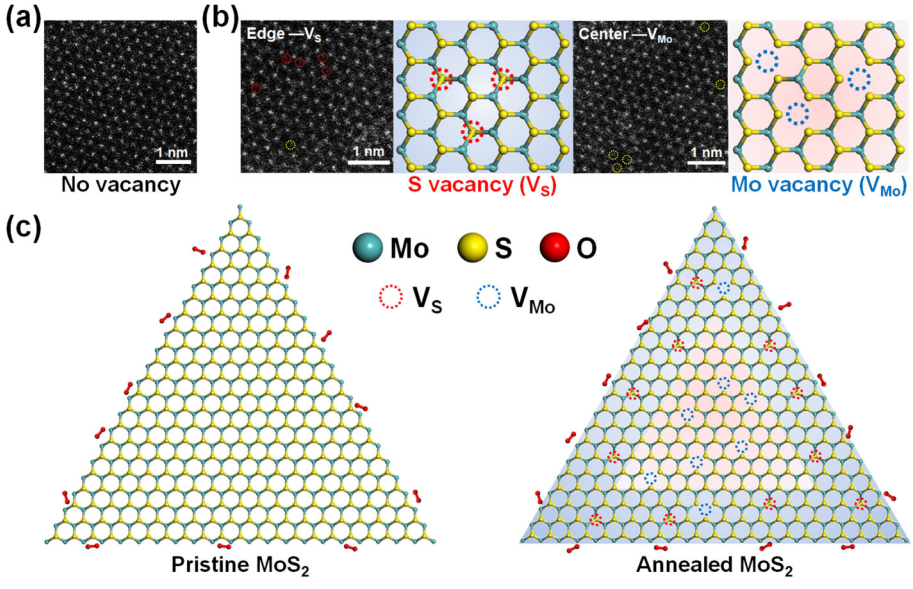

Figure 5 Patterned heterogeneous defect domains in CVD-synthesized MoS_2. (a) STEM image of pristine MoS_2. (b) STEM image of annealed MoS_2, where V_S and V_{Mo} are marked by red and blue circles, respectively. (c) Schematic of heterogeneous defect domains in pristine and annealed MoS_2.

that observed in the V_S-rich regions (Fig. 5(c)), likely attributed to enhanced O_2 adsorption at the Mo-edge suppressed nonradiative recombination, thereby amplifying the emission, in agreement with prior reports of edge-dominated behavior [58].

Electrocatalytic and photoelectrocatalytic measurements further highlighted these spatial variations: during electrocatalysis, the central region of annealed MoS_2 showed prominent ECL signals, while photoelectrocatalysis induced a significant negative shift in PECL onset potential (from +0.2 to −0.2 V) compared to pristine MoS_2. V_{Mo}, concentrated at the center, likely induces local p-type characteristics and enhances catalytic charge transfer, contributing to the central ECL signal. V_S, enriched at edges, enhanced photocatalytic efficiency through electronic effects: they introduced band gap defect levels to boost light absorption and trap electrons, promoting electron–hole separation and channeling more holes to drive OER [60] (distinct from their direct HER role [61]), which accounted for the enhanced PEC activity and onset potential shift.

Moreover, a key consideration for practical application lies in the balance between activity and stability. Under illumination, photogenerated h^+ are channeled to catalytic sites to drive OER, but these highly reactive species may also participate in undesired side reactions, potentially leading to material degradation. Both pristine and annealed MoS_2 exhibited noticeable corrosion in regions where PECL was readily generated, whereas no noticeable material corrosion occurred under the dark conditions. This spatial correlation strongly suggests that the sites driving PEC activity are also preferential targets for photo-corrosion, underscoring the inherent trade-off between activity and stability—a core challenge in TMDs-based photoanode development.

Mechanistically, the regions exhibiting strong PECL signals correspond to zones with high hole accumulation, where photogenerated h^+ rapidly oxidize adsorbed water molecules to drive OER. However, these same reactive holes can also attack the Mo–S bonds, particularly near defect-rich domains, resulting in oxidative etching and photo-corrosion. The concurrent enhancement in activity and corrosion thus reflects a competitive process between productive oxygen evolution and destructive lattice oxidation, which must be balanced through passivation or protective coatings in future designs.

3 Conclusions

A multimodal *in situ* ECL/PECL/PL and *ex situ* STEM strategy was used to directly observe the electro- and photoelectrocatalytic behavior of 2D materials, enabling simultaneous spatiotemporal resolution of the active sites and carrier dynamics and identification of catalytically active sites at the atomic level. By deploying the new *in situ* platform on p-type WSe_2 and n-type MoS_2, we directly demonstrate how majority carriers drive electrocatalysis while photogenerated minority carriers mediate photoelectrocatalysis. Using the multi-resolved approach, CVD-synthesized pristine and annealed monolayer MoS_2 nanosheets were comprehensively studied under electrocatalytic and photoelectrocatalytic conditions. The pristine MoS_2 exhibited low electrocatalytic activity, high photoelectrocatalytic activity in the center, and a high PL signal at the edge, whereas the annealed MoS_2 exhibited high electrocatalytic activity in the center, high photoelectrocatalytic activity, and a strong PL signal at the edge. The STEM results revealed the formation of V_{Mo} throughout the nanosheets and V_S primarily at the edge after annealing. Correlation analysis highlighted the role of V_{Mo} as the catalytic center in both modes and the promotional effect of V_S on the photoelectrocatalytic properties.

These findings suggest a clear design principle for next-generation defect-engineered catalysts: intentionally introducing a spatially controlled distribution of V_{Mo} and V_S could enable synergistic optimization of both catalytic activity and light-harvesting efficiency. A key challenge remains in balancing this enhanced OER activity with TMD stability, which may be addressed by strategic defect engineering such as selective passivation, dopant incorporation, or core–shell structuring to protect metastable active sites. Tailored synthesis strategies such as controlled annealing, plasma treatment, or precursor modulation may thus be developed to precisely tune defect types and densities for optimal performance. This study provides a multi-perspective approach for obtaining shared and unique underlying mechanisms across different catalytic modes on the same materials at electrochemical interfaces, which can aid in the rational design of more efficient catalysts for energy conversion.

Electronic Supplementary Material: Supplementary material (detailed preparation methods for optoelectrochemical cell and experimental setup; additional characterization results, including AFM images, mechanistic pathways analysis, optical microscope images, and intensity analysis; and additional performances, such as CV, *in situ* PL spectrum, PL mapping, and Raman mapping) is available in the online version of this article at https://doi.org/10.26599/NR.2026.94908340.

Data availability

All data needed to support the conclusions in the paper are presented in the manuscript and the Electronic Supplementary Material. Additional data related to this paper may be requested from the corresponding author upon request.

Acknowledgements

This work was financially supported by the National Natural Science Foundation of China (Nos. 22374064 and 22175060) and the Shenzhen Innovation of Science and Technology Commission (No. ZDSYS20230626090803004).

Declaration of competing interest

All the contributing authors report no conflict of interests in this work.

Author contribution statement

R. H. and S. L. conceived and supervised the project, and procured the funding. L. S. W. performed the imaging and electrochemical experiments. Z. J. D. and J. Y. C. performed the synthetic experiment and structural studies. L. S. W., H. K. C., and B. L. analyzed the data. The paper was written with input from all authors. All authors discussed the results in detail and commented on the manuscript.

Use of AI statement

None.

References

[1] Yao, T. T.; An, X. R.; Han, H. X.; Chen, J. Q.; Li, C.

Photoelectrocatalytic materials for solar water splitting. *Adv. Energy Mater.* **2018**, *8*, 1800210.

[2] Niu, S. W.; Cai, J. Y.; Wang, G. M. Two-dimensional MoS_2 for hydrogen evolution reaction catalysis: The electronic structure regulation. *Nano Res.* **2021**, *14*, 1985–2002.

[3] Mefford, J. T.; Akbashev, A. R.; Kang, M.; Bentley, C. L.; Gent, W. E.; Deng, H. D.; Alsem, D. H.; Yu, Y. S.; Salmon, N. J.; Shapiro, D. A. et al. Correlative *operando* microscopy of oxygen evolution electrocatalysts. *Nature* **2021**, *593*, 67–73.

[4] Zhang, W. D.; Chen, S. R.; Shen, K.; Zhu, J.; Liu, Y.; Mao, X. W. Understanding photo(electro)catalysts for energy conversion via *operando* functional imaging. *Chem. Biomed. Imaging* **2023**, *1*, 522–536.

[5] Xu, Y.; Ge, R. Y.; Yang, J.; Li, J. C.; Li, S. A.; Li, Y.; Zhang, J. J.; Feng, J.; Liu, B.; Li, W. X. Molybdenum disulfide (MoS_2)-based electrocatalysts for hydrogen evolution reaction: From mechanism to manipulation. *J. Energy Chem.* **2022**, *74*, 45–71.

[6] Chi, Z. X.; Zhao, J. Y.; Zhang, Y.; Yu, H.; Yu, H. B. The fabrication of atomically thin-MoS_2 based photoanodes for photoelectrochemical energy conversion and environment remediation: A review. *Green Energy Environ.* **2022**, *7*, 372–393.

[7] Yu, X. Y.; Guijarro, N.; Johnson, M.; Sivula, K. Defect mitigation of solution-processed 2D WSe_2 nanoflakes for solar-to-hydrogen conversion. *Nano Lett.* **2018**, *18*, 215–222.

[8] Sun, Y.; Zhang, X. W.; Mao, B. G.; Cao, M. H. Controllable selenium vacancy engineering in basal planes of mechanically exfoliated WSe_2 monolayer nanosheets for efficient electrocatalytic hydrogen evolution. *Chem. Commun.* **2016**, *52*, 14266–14269.

[9] Liu, D. Q.; Zhang, B. X.; Zhao, G. Q.; Chen, J.; Pan, H. G.; Sun, W. P. Advanced *in-situ* electrochemical scanning probe microscopies in electrocatalysis. *Chin. J. Catal.* **2023**, *47*, 93–120.

[10] Tarnev, T.; Aiyappa, H. B.; Botz, A.; Erichsen, T.; Ernst, A.; Andronescu, C.; Schuhmann, W. Scanning electrochemical cell microscopy investigation of single ZIF-derived nanocomposite particles as electrocatalysts for oxygen evolution in alkaline media. *Angew. Chem., Int. Ed.* **2019**, *58*, 14265–14269.

[11] Daviddi, E.; Gaudin, L. F.; Bentley, C. L. Scanning electrochemical cell microscopy: High-resolution structure–property studies of mono- and polycrystalline electrode materials. *Curr. Opin. Electrochem.* **2022**, *34*, 101006.

[12] Liberman, I.; He, W. H.; Shimoni, R.; Ifraemov, R.; Hod, I. Spatially confined electrochemical conversion of metal-organic frameworks into metal-sulfides and their *in situ* electrocatalytic investigation via scanning electrochemical microscopy. *Chem. Sci.* **2020**, *11*, 180–185.

[13] Saqib, M.; Fan, Y. S.; Hao, R.; Zhang, B. Optical imaging of nanoscale electrochemical interfaces in energy applications. *Nano Energy* **2021**, *90*, 106539.

[14] Hao, R.; Fan, Y. S.; Howard, M. D.; Vaughan, J. C.; Zhang, B. Imaging nanobubble nucleation and hydrogen spillover during electrocatalytic water splitting. *Proc. Natl. Acad. Sci. USA* **2018**, *115*, 5878–5883.

[15] Wang, W. K.; Chen, J. J.; Lou, Z. Z.; Kim, S.; Fujitsuka, M.; Yu, H. Q.; Majima, T. Single-molecule and -particle probing crystal edge/corner as highly efficient photocatalytic sites on a single TiO_2 particle. *Proc. Natl. Acad. Sci. USA* **2019**, *116*, 18827–18833.

[16] Hao, R.; Fan, Y. S.; Anderson, T. J.; Zhang, B. Imaging single nanobubbles of H_2 and O_2 during the overall water electrolysis with single-molecule fluorescence microscopy. *Anal. Chem.* **2020**, *92*, 3682–3688.

[17] Hu, S.; Yi, J.; Zhang, Y. J.; Lin, K. Q.; Liu, B. J.; Chen, L.; Zhan, C.; Lei, Z. C.; Sun, J. J.; Zong, C. et al. Observing atomic layer electrodeposition on single nanocrystals surface by dark field spectroscopy. *Nat. Commun.* **2020**, *11*, 2518.

[18] Xu, S. H.; Yu, X. R.; Chen, Z. H.; Zeng, Y. B.; Guo, L. H.; Li, L.; Luo, F.; Wang, J.; Qiu, B.; Lin, Z. Y. Real-time visualization of the single-nanoparticle electrocatalytic hydrogen generation process and activity under dark field microscopy. *Anal. Chem.* **2020**, *92*, 9016–9023.

[19] Mao, J. X.; Li, G. P.; Saqib, M.; Xu, J. T.; Hao, R. Super-resolved dynamics of isolated zinc formation during extremely fast electrochemical deposition/dissolution processes. *Chem. Sci.* **2022**, *13*, 12782–12790.

[20] Wang, Y. X.; Shan, X. N.; Wang, H.; Wang, S. P.; Tao, N. J. Plasmonic imaging of surface electrochemical reactions of single gold nanowires. *J. Am. Chem. Soc.* **2017**, *139*, 1376–1379.

[21] Wang, Y. J.; Jiang, Y. Y.; Wang, W. Determining the subnanometer thickness of the water-depletion layer at the interface between water and the hydrophobic substrate. *Anal. Chem.* **2019**, *91*, 11696–11702.

[22] Chen, M. M.; Xu, C. H.; Zhao, W.; Chen, H. Y.; Xu, J. J. Super-resolution electrogenerated chemiluminescence microscopy for single-nanocatalyst imaging. *J. Am. Chem. Soc.* **2021**, *143*, 18511–18518.

[23] Dong, J. R.; Xu, Y.; Zhang, Z. Q.; Feng, J. D. *Operando* imaging of chemical activity on gold plates with single-molecule electrochemiluminescence microscopy. *Angew. Chem., Int. Ed.* **2022**, *61*, e202200187.

[24] Chen, Y.; Zhao, D. B.; Fu, J. J.; Gou, X. D.; Jiang, D. C.; Dong, H.; Zhu, J. J. *In situ* imaging facet-induced spatial heterogeneity of electrocatalytic reaction activity at the subparticle level via electrochemiluminescence microscopy. *Anal. Chem.* **2019**, *91*, 6829–6835.

[25] Chen, M. M.; Zhao, W.; Zhu, M. J.; Li, X. L.; Xu, C. H.; Chen, H. Y.; Xu, J. J. Spatiotemporal imaging of electrocatalytic activity on single 2D gold nanoplates via electrogenerated chemiluminescence microscopy. *Chem. Sci.* **2019**, *10*, 4141–4147.

[26] Zhang, Y.; Xiao, J. W.; Xie, X.; Chen, H. J.; Deng, S. Z. Layer dependence of the photoelectrochemical performance of a WSe_2 photocathode characterized using *in situ* microscale measurements. *RSC Adv.* **2019**, *9*, 30925–30931.

[27] Sambur, J. B.; Chen, T. Y.; Choudhary, E.; Chen, G. Q.; Nissen, E. J.; Thomas, E. M.; Zou, N. M.; Chen, P. Sub-particle reaction and photocurrent mapping to optimize catalyst-modified photoanodes. *Nature* **2016**, *530*, 77–80.

[28] Shen, M. K.; Ding, T. B.; Hartman, S. T.; Wang, F. D.; Krucylak, C.; Wang, Z. Y.; Tan, C.; Yin, B.; Mishra, R.; Lew, M. D. et al. Nanoscale colocalization of fluorogenic probes reveals the role of oxygen vacancies in the photocatalytic activity of tungsten oxide nanowires. *ACS Catal.* **2020**, *10*, 2088–2099.

[29] Mao, X. W.; Chen, P. Inter-facet junction effects on particulate photoelectrodes. *Nat. Mater.* **2022**, *21*, 331–337.

[30] Wen, L.; Chen, H. K.; Hao, R. Wide-field imaging of active site distribution on semiconducting transition metal dichalcogenide nanosheets in electrocatalytic and photoelectrocatalytic processes. *Chem. Sci.* **2024**, *15*, 16778–16788.

[31] Zhao, Y. R.; Yu, J.; Xu, G. B.; Sojic, N.; Loget, G. Photoinduced electrochemiluminescence at silicon electrodes in water. *J. Am. Chem. Soc.* **2019**, *141*, 13013–13016.

[32] Yu, J.; Saada, H.; Abdallah, R.; Loget, G.; Sojic, N. Luminescence amplification at $BiVO_4$ photoanodes by photoinduced electrochemiluminescence. *Angew. Chem., Int. Ed.* **2020**, *59*, 15157–15160.

[33] Yu, J.; Saada, H.; Sojic, N.; Loget, G. Photoinduced electrochemiluminescence at nanostructured hematite electrodes. *Electrochim. Acta* **2021**, *381*, 138238.

[34] Zhao, Y. R.; Bouffier, L.; Xu, G. B.; Loget, G.; Sojic, N. Electrochemiluminescence with semiconductor (nano)materials. *Chem. Sci.* **2022**, *13*, 2528–2550.

[35] Xue, J. W.; Xu, C. H.; Zhao, W.; Chen, H. Y.; Xu, J. J. Photoinduced electrogenerated chemiluminescence imaging of plasmonic photoelectrochemistry at single nanocatalysts. *Nano Lett.* **2023**, *23*, 4572–4578.

[36] Jing, L. Q.; Qu, Y. C.; Wang, B. Q.; Li, S. D.; Jiang, B. J.; Yang, L. B.; Fu, W.; Fu, H. G.; Sun, J. Z. Review of photoluminescence performance of nano-sized semiconductor materials and its

relationships with photocatalytic activity. *Solar Energy Mater. Solar Cells* **2006**, *90*, 1773–1787.

[37] Lee, Y.; Park, S.; Kim, H.; Han, G. H.; Lee, Y. H.; Kim, J. Characterization of the structural defects in CVD-grown monolayered MoS_2 using near-field photoluminescence imaging. *Nanoscale* **2015**, *7*, 11909–11914.

[38] Zhang, K. H.; Wang, Y. X.; Joshi, J.; Zhang, F.; Subramanian, S.; Terrones, M.; Vora, P.; Crespi, V.; Robinson, J. A. Probing the origin of lateral heterogeneities in synthetic monolayer molybdenum disulfide. *2D Mater.* **2019**, *6*, 025008.

[39] Hou, C.; Deng, J. W.; Guan, J. X.; Yang, Q. R.; Yu, Z. H.; Lu, Y. L.; Xu, Z. H.; Yao, Z. F.; Zheng, J. R. Photoluminescence of monolayer MoS_2 modulated by water/O_2/laser irradiation. *Phys. Chem. Chem. Phys.* **2021**, *23*, 24579–24588.

[40] Cui, Y.; Zhao, X.; Saqib, M.; Hao, R. Multimode imaging analysis of single particles at the electrochemical interfaces. *Curr. Opin. Electrochem.* **2024**, *46*, 101527.

[41] Mao, J. X.; Wu, B. H.; Hao, R. Imaging the 4D chemical heterogeneity of single V_2O_5 particles during charging/discharging processes. *Adv. Mater.* **2025**, *37*, 2501425.

[42] Zhao, X.; Li, Y. Y.; Cui, Y.; Saqib, M.; Zhang, X. Y.; Hao, R.; Zheng, Z. P. Spatiotemporally and chemically resolved imaging of electrocatalytic oxygen evolution on single nanoplates of cobalt-layered hydroxide. *J. Am. Chem. Soc.* **2023**, *145*, 20897–20906.

[43] Zhao, X.; Chen, H. K.; Cui, Y.; Zhang, X. Y.; Hao, R. Dual-mode imaging of dynamic interaction between bubbles and single nanoplates during the electrocatalytic hydrogen evolution process. *Small* **2024**, *20*, 2400273.

[44] Lu, C. P.; Li, G. H.; Mao, J. H.; Wang, L. M.; Andrei, E. Y. Bandgap, mid-gap states, and gating effects in MoS_2. *Nano Lett.* **2014**, *14*, 4628–4633.

[45] Cheng, Q. L.; Pang, J. B.; Sun, D. H.; Wang, J. G.; Zhang, S.; Liu, F.; Chen, Y. K.; Yang, R. Q.; Liang, N.; Lu, X. H. et al. WSe_2 2D p-type semiconductor-based electronic devices for information technology: Design, preparation, and applications. *InfoMat* **2020**, *2*, 656–697.

[46] Vogel, Y. B.; Darwish, N.; Ciampi, S. Spatiotemporal control of electrochemiluminescence guided by a visible light stimulus. *Cell Rep. Phys. Sci.* **2020**, *1*, 100107.

[47] Han, X. X.; Li, Y. B.; Li, D.; Liu, C. Role of free radicals/reactive oxygen species in MeHg photodegradation: Importance of utilizing appropriate scavengers. *Environ. Sci. Technol.* **2017**, *51*, 3784–3793.

[48] Wei, Y. J.; Fan, X. C.; Chen, D. X.; Zhu, X. N.; Yao, L.; Zhao, X.; Tang, X.; Wang, J. W.; Zhang, Y. J.; Qiu, T. et al. Probing oxidation mechanisms in plasmonic catalysis: Unraveling the role of reactive oxygen species. *Nano Lett.* **2024**, *24*, 2110–2117.

[49] Chen, R.; Wang, X.; Wu, K. Q.; Liu, S. Q.; Zhang, Y. J. Voltammetric study and modeling of the electrochemical oxidation process and the adsorption effects of luminol and luminol derivatives on glassy carbon electrodes. *Anal. Chem.* **2022**, *94*, 17625–17633.

[50] Chia, X.; Eng, A. Y. S.; Ambrosi, A.; Tan, S. M.; Pumera, M. Electrochemistry of nanostructured layered transition-metal dichalcogenides. *Chem. Rev.* **2015**, *115*, 11941–11966.

[51] Splendiani, A.; Sun, L.; Zhang, Y. B.; Li, T. S.; Kim, J.; Chim, C. Y.; Galli, G.; Wang, F. Emerging photoluminescence in monolayer MoS_2. *Nano Lett.* **2010**, *10*, 1271–1275.

[52] Lien, D. H.; Uddin, S. Z.; Yeh, M.; Amani, M.; Kim, H.; Ager, J. W.; Yablonovitch, E.; Javey, A. Electrical suppression of all nonradiative recombination pathways in monolayer semiconductors. *Science* **2019**, *364*, 468–471.

[53] Nan, H. Y.; Wang, Z. L.; Wang, W. H.; Liang, Z.; Lu, Y.; Chen, Q.; He, D. W.; Tan, P. H.; Miao, F.; Wang, X. R. et al. Strong photoluminescence enhancement of MoS_2 through defect engineering and oxygen bonding. *ACS Nano* **2014**, *8*, 5738–5745.

[54] Yang, P. F.; Zou, X. L.; Zhang, Z. P.; Hong, M.; Shi, J. P.; Chen, S. L.; Shu, J. P.; Zhao, L. Y.; Jiang, S. L.; Zhou, X. B. et al. Batch production of 6-inch uniform monolayer molybdenum disulfide catalyzed by sodium in glass. *Nat. Commun.* **2018**, *9*, 979.

[55] Wang, H. G.; Zhu, X. K.; Zhao, Z. Y.; Wang, X. S.; Qian, Z. Y.; Jiao, L. Y.; Wang, K. K.; Li, Y.; Qi, J. J.; Asif, M. et al. *In situ* imaging of two-dimensional crystal growth using a heat-resistant optical microscope. *Nano Lett*. **2024**, *24*, 5498–5505.

[56] Liu, Y. Y.; Stradins, P.; Wei, S. H. Air passivation of chalcogen vacancies in two-dimensional semiconductors. *Angew. Chem., Int. Ed.* **2016**, *55*, 965–968.

[57] Luo, Z. Y.; Zheng, W. H.; Luo, N. N.; Liu, B.; Zheng, B. Y.; Yang, X.; Liang, D. L.; Qu, J. Y.; Liu, H. W.; Chen, Y. et al. Photoluminescence lightening: Extraordinary oxygen modulated dynamics in WS_2 monolayers. *Nano Lett.* **2022**, *22*, 2112–2119.

[58] Kumar, A.; Kumar, P.; Chouksey, A.; Lal, M.; Laishram, R.; Singh, A.; Rawat, J. S.; Jain, A. Photoluminescence enhancement of CVD-grown MoS_2 monolayer by p-type doping using oxygen annealing technique. *J. Electron. Mater.* **2025**, *54*, 2229–2238.

[59] Wang, Z. Y.; Chen, J.; Ni, C. W.; Nie, W.; Li, D. F.; Ta, N.; Zhang, D. Y.; Sun, Y. M.; Sun, F. S.; Li, Q. et al. Visualizing the role of applied voltage in non-metal electrocatalysts. *Natl. Sci. Rev.* **2023**, *10*, nwad166.

[60] Ren, Z. X.; Li, Y.; Ren, Q. Y.; Zhang, X. J.; Fan, X. F.; Liu, X. J.; Fan, J. C.; Shen, S. L.; Tang, Z. H.; Xue, Y. H. Unveiling the role of sulfur vacancies in enhanced photocatalytic activity of hybrids photocatalysts. *Nanomaterials* **2024**, *14*, 1009.

[61] Li, X. Y.; Zhu, S. J.; Wang, Y. L.; Lian, T.; Yang, X. Y.; Ye, C. F.; Li, Y.; Su, B. L.; Chen, L. H. Synergistic regulation of S-vacancy of MoS_2-based materials for highly efficient electrocatalytic hydrogen evolution. *Front. Chem.* **2022**, *10*, 915468.